DOI: 10.1002/ ((please add manuscript number))
Article type: Full Paper

In situ Investigations on the Structural and Morphological Changes of Metal Phosphides as Anode Materials in Lithium-Ion Batteries

Xin He, Rui Wang, Marian Cristian Stan, Elie Paillard, Jun Wang, Henrich Frielinghaus\*, Jie Li\*

X. He, Dr. M. C. Stan, Dr. J. Wang, Dr. J. Li

MEET Battery Research Center, Institute of Physical Chemistry, University of Münster, Corrensstraße 46, D-48149 Münster, Germany

E-mail: jie.li@uni-muenster.de

X. He, Dr. E. Paillard

Helmholtz Institute Münster – Forschungszentrum Jülich GmbH (IEK 12), Corrensstraße 46, 48149 Münster, D-48149 Münster, Germany.

R. Wang, Dr. H. Frielinghaus

Jülich Centre for Neutron Science at MLZ, Forschungszentrum Jülich GmbH,

Lichtenbergstrasse 1, D-85747 Garching, Germany.

E-mail: h.frielinghaus@fz-juelich.de

Keywords: metal phosphides, structural and morphological changes, lithium-ion batteries, conversion, alloying

The binary metal phosphides (M-P, M= Cu, Fe, Sn, Sb) compounds are of great interest as negative electrode materials for high energy density lithium-ion batteries. However, the morphology and structural changes at the nanoscale upon electrochemical (de)lithiation are not clear yet, which require further detailed investigation. In situ neutron scattering technique was utilized to investigate and compare the morphological changes of copper phosphide and tin phosphide during the initial cycle. By coupling with SEM investigation, the surface activities of the electrodes at different electrochemical state, including the SEI formation, swelling and recovering, cracks appearance and stripping at nanoscale of the material particles are evaluated. With in situ XRD measurement, the energy storage mechanism was further explained. This work demonstrates useful techniques to analyze the detailed fatigue mechanisms of the active material, and provides new insights of the nanostructural changes of anode materials reacting with lithium via conversion and alloying.

#### 1. Introduction

The binary metal phosphides (M-P) compounds have gained extensive attention for sustainable energy applications, including as catalysts for hydrogen evolution [1-7] and as anode materials for lithium-ion batteries. Especially in the lithium ion batteries, these binary M-P compounds attract recent research interests due to their promising Li-storage properties. The M-P compounds exhibit high degree of electron delocalization, where the redox centers are located on the bands contributed by the metal cation and phosphorus anion due to the strong covalent character of M-P bond. Based on this, the Li-storage mechanism of  $M_x P_y$  nanocomposite materials can be classified into two different classes: Li intercalation and conversion reactions. The conversion reaction can be further divided

into two types, metallization and metal alloying. [9, 16] In the case of metallization, Li ions first insert into the lattice of phosphorus-based materials to form  $Li_nM_xP_v$  at low lithiation states, [12, <sup>17]</sup> then the nanosized metallic particles  $(M^0)$  are decomposed and lithium phosphide (such as Li<sub>3</sub>P) is formed as the reaction continues. Further lithium uptake is not possible, which means that the lithium does not form intermetallic compounds with M<sup>0</sup> phase and the electrochemical lithiation is complete. As an example, the Cu<sub>3</sub>P material shows the theoretical specific capacity of 363 mAh g $^{-1}$  according to this mechanism. $^{[18,19]}$  In contrast , other  $M_x P_v$ compounds in which both M and P are able to react with lithium to form Li<sub>n</sub>M and Li<sub>3</sub>P<sup>[20,21]</sup>, the M<sup>0</sup> formed via metallization reaction reacts further with Li to form intermetallic allovs. [14] This metal alloying process allows for higher capacities compared to the metallization mechanism, Sn<sub>4</sub>P<sub>3</sub> for instance, delivers a theoretical capacity of 1255 mAh g<sup>1</sup> corresponding to the formation of Li<sub>3</sub>P and Li<sub>22</sub>Sn<sub>5</sub> as the final products. The well-dispersed Li<sub>3</sub>P phase provides a shielding matrix to prevent the aggregation of the Li<sub>n</sub>M/M nanoparticles, thus improving the cycling stability of the metal phosphide anode. [22] The resulting Lin alloy then acts as a conducting pathway to facilitate the reversible Li storage reaction. [23] Unfortunately, these materials still suffer from relatively large irreversible capacities and structural collapse caused by the large volume change occurred during (de)lithiation process. Moreover, the formation of dendrites after several cycles poses a grievous safety issue. In order to improve the electrochemical performance of M<sub>x</sub>P<sub>y</sub> compounds, morphology tailoring has been proved to be an efficient way. [24] However, how the morphology affect the electrochemical process of these materials is not clear, calling for deeper investigation. Some efforts have been devoted in investigating variations of the active materials. For example, using scanning electron microscopy (SEM)<sup>[25]</sup> and transmission electron microscopy (TEM)<sup>[26]</sup> measurements, a clear evidence of the volume expansion and solid electrolyte interphase (SEI) formation was provided. However, both techniques are not able to give a quantitative value of such changes at real time. Since volume expansion, as the accumulated effect of nanostructural evolution, can lead to strain-induced fractures and further degrade the electrochemical performance of active materials, a quantitative investigation on the nanostructure changes of M<sub>x</sub>P<sub>v</sub> compounds during electrochemical lithiation is a key aspect for understanding the fundamental mechanism. Small angle neutron scattering (SANS) has been applied to investigate the changes of the nanostructure (such as size, volume and shape of particles) via using high penetration depth. [27] Thus, combination of SANS and electrochemical testing is a non-invasive method for monitoring morphology changes during electrochemical cycling, including the volumic expansion and the generation of fractures. In this work, Cu<sub>3</sub>P and Sn<sub>4</sub>P<sub>3</sub> active materials were prepared via a wet mechanochemical method. In situ SANS was employed to evaluate the electrochemical swelling and recovery of the individual nanoscale grains for these anode materials. The morphological changes can be detected and quantified by recording spectrum at a certain intervals. Furthermore, SEM and in situ powder X-ray diffraction (XRD) were also carried out to complement the SANS data. Phase transition accompanied by detailed aging mechanisms during electrochemical process was further evaluated.

### 2. Results and discussion

The particle morphologies and elemental distributions of the synthesized  $Cu_3P$  and  $Sn_4P_3$  materials were characterized by SEM and energy-dispersive X-ray spectroscopy (EDX), and the results are shown in Figure 1. Both samples are composed of micro-particles, agglomerating with each other, in the range between 0.2 to 4 " m (Figure 1a and 1e). Figure 1b and 1c shows that the elemental distribution of Cu and P elements in  $Cu_3P$  is homogeneous. A small amount of electrochemically inactive W (originating from the ball milling jars and balls used to carry out the synthesis), as shown in Figure 1d, was presented in the  $Cu_3P$ 

sample. Figure 1f and 1g exhibit that Sn and P elements are distributed uniformly in the  $Sn_4P_3$  sample. The W element can be also observed, as shown in Figure 1h.

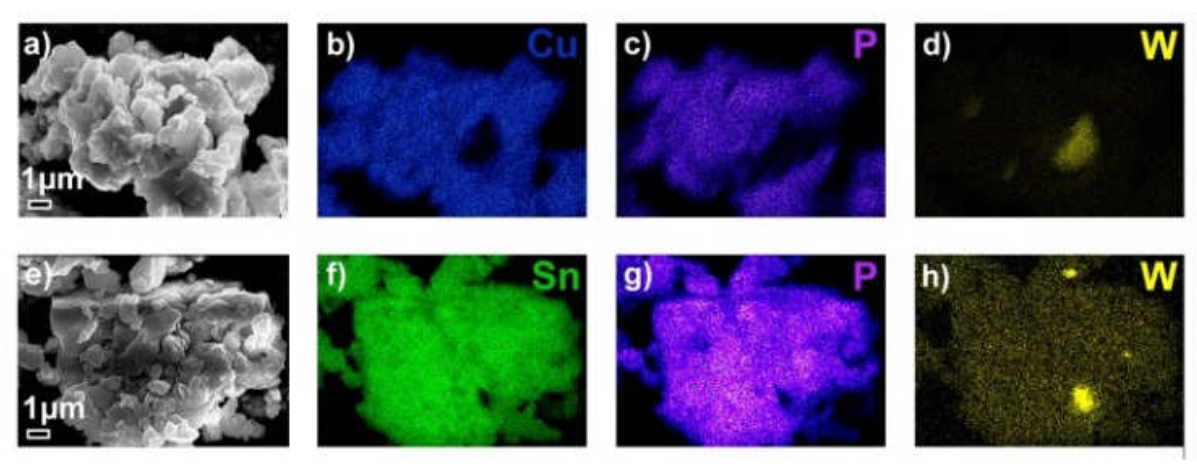


Figure 1. (a) SEM image of the  $Cu_3P$  pristine material and corresponding EDX mapping images of (b) Cu, (c) P and (d) W elements, respectively. (e) SEM image of the  $Sn_4P_3$  material and corresponding EDX mapping images of the (f) Sn, (g) P and (h) W elements, respectively.

The crystallographic structure of the  $Cu_3P$  sample was characterized by XRD, and the powder pattern is shown in Figure 2a. The main diffraction peaks can be assigned to a hexagonal structure with space group of  $P6_3$ cm (PDF No. 04-010-6017).  $^{[19,\ 28]}$  A small quantity of tungsten carbide (WC), marked with asterisks can be observed in this case. The presence of WC originating from the ball milling jars and balls is also observed. Figure 2b exhibits the XRD pattern of the  $Sn_4P_3$  samples. The main diffraction peaks can be indexed as a hexagonal structure with R-3m space group (PDF No. 04-003-2006).  $^{[22,\ 29]}$  Small amount of WC phase was also identified in this sample, marked with asterisks as well. According to EDX measurement, the amount of the WC impurities are 4.8% and 1.2% (weight ratio) in  $Cu_3P$  and  $Sn_4P_3$  samples, respectively. In both final products, no unreacted metallic copper or tin can be detected which means that the reaction from the starting reagents to stoichiometric amounts of the  $Cu_3P$  or  $Sn_4P_3$  components is completed after 15 hours of synthesis.

A schematic illustration of the hexagonal Cu<sub>3</sub>P crystal structure is presented in Figure 2a. It can be viewed as an alternate stacking of different types of atomic layers in the c-axis. One type is a puckered layer of six-membered rings constructed only by copper neighbors while Copper and phosphorus atoms constitute another type of layer, intercalating and connecting the puckered layers. Four types of copper atoms occupy the neighbor sites around each phosphorous atom. Cu1 is located in a distorted tetrahedron with four adjacent phosphorus atoms and eight copper neighbors; Cu2 is sited in a tetrahedral arrangement with four adjacent phosphorus atoms and nine copper neighbors; both Cu3 and Cu4 are sited in a trigonal pyramidal coordination with three adjacent phosphorus atoms and nine copper neighbors. [30] The hexagonal Sn<sub>4</sub>P<sub>3</sub> structure consists of alternative layers of tin and phosphorus atoms that are grouped into seven-layer blocks, and these blocks propagate along the c-axis (Figure 2b). All the phosphorus atoms are located in the center of the tetragonal structure. Meanwhile, they are octahedrally coordinated by six tin atoms. There are two types of tin atoms in the crystal structure. Sn1 is octahedrally coordinated by phosphorus atoms; Sn2 has a [3 + 3] coordination with three phosphorus atoms on one side and three Sn2 atoms from the adjacent block. Within each block, the Sn1: Sn2 ratio is 1:1. [31]

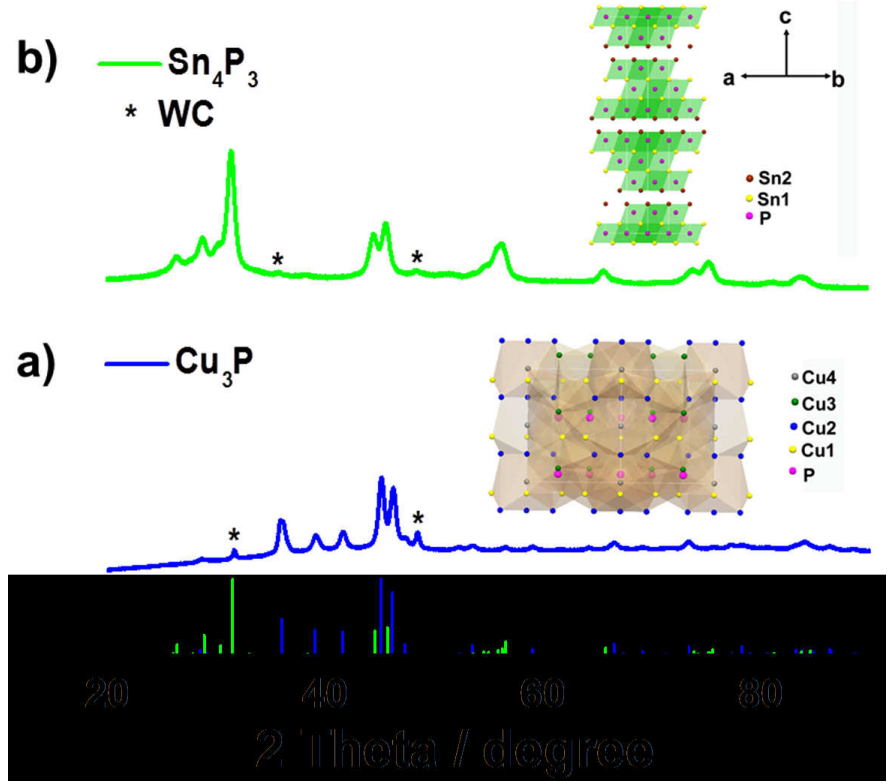
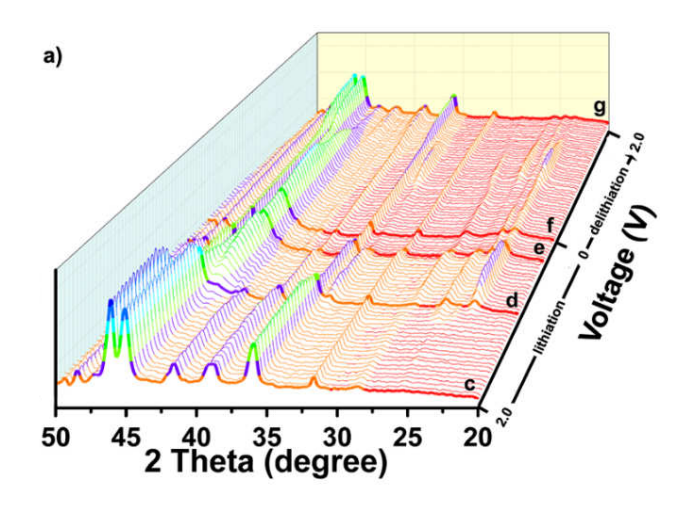
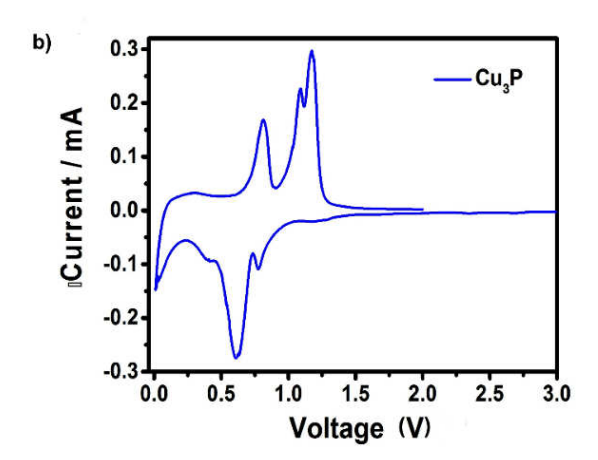


Figure 2. XRD diffraction patterns and schematic illustration of hexagonal  $Cu_3P$  (a) and  $Sn_4P_3$  (b) samples.

In order to elucidate the structure evolution of Cu<sub>3</sub>P, in-situ XRD analysis was carried out to investigate the first lithiation/delithiation process. XRD patterns acquired within 2.045 - 0.01V are displayed in Figure 3a, while the 1<sup>st</sup>, 22<sup>nd</sup>, 38<sup>th</sup>, 46<sup>th</sup> and 90<sup>th</sup> scans, corresponding to of 2.0, 1.0, 0.36, 0.01 and 2.0 V are shown in Figure 3c, 3d, 3e 3f and 3g, respectively. The cyclic voltammogram for a pristine Cu<sub>3</sub>P electrode is presented in Figure 3b. During the cathodic potential sweep from 1.1 V to 0.01 V, four distinct cathodic peaks are observed: a small peak at 0.78 V, an intense peak at 0.63 V, a weak broad peak at 0.41 V, and a broad peak below 0.2 V, respectively. During the anodic sweep, only three anodic current peaks are noticed: a peak at 0.81 V, two overlapping peaks at 1.09 V and 1.17 V in the potential range from 0.01 V to 2.0 V. It can be confirmed that there are no structural changes occurring when the voltage decreases from the pristine state (OCV) until to 1.2 V during the lithiation process (Figure 3a). As the voltage decreases, the intensity of the Cu<sub>3</sub>P characteristic peaks declines, and several new peaks arise, which can be ascribed to the formation of the Li<sub>2</sub>CuP phase. It is proved by the 22<sup>nd</sup> diffraction pattern at the voltage of ~1.0 V, shown in Figure 3d. An LiCu<sub>2</sub>P intermediate phases may be formed before the origination of Li<sub>2</sub>CuP, <sup>[32]</sup> though it was not detected in the present work. The reason could be that the disordered structure of LiCu<sub>2</sub>P phase makes it difficult to be detected by XRD. These reactions complete at the voltage of 0.5 V, which corresponds to the first two peaks in the CV curve. The redox peaks can be seen at 1.09 V and 1.17 V in the anodic sweep. As the lithiation process goes on, Li<sub>2</sub>CuP phase is reduced, and the peaks for the Li<sub>3</sub>P and Cu phases appear, as shown in Figure 3a and 3e. The third peak at 0.41 V in CV curve corresponds to this process, and the anodic peak corresponding to the reverse reaction appears at 0.81 V. At the end of the lithiation process (0.01 V), the diffraction peaks of Li<sub>3</sub>P and Cu<sup>0</sup> shown in Figure 3f, remain and the ones of Li<sub>2</sub>CuP almost disappear indicating the almost complete electrochemical reaction. The fourth peak (below 0.2 V) in the CV curve is associated with SEI formation and the irreversible changes occurring only during the first discharge since there has no corresponding anodic peak. During the delithiation process, the reverse phase transitions can be observed at 2.0V that the main diffraction peaks can be signed to Cu<sub>3</sub>P, as shown in Figure 3g. In other words,

the recovering of the  $Cu_3P$  phase after the first lithiation/delithiation process gives an indication on the good stability of the material structure upon electrochemical lithiation. However, a small trace of the  $Li_2CuP$  phase can be still observed, indicating that a small part of Li ions have irreversibly reacted during the first cycle. These observations are in good agreement with the recently published work of Poli et al. that a disordered  $Li_2CuP$  phase is formed at the end of the delithiation process which was proved by  $^7Li$  and  $^{31}P$  NMR measurements.  $^{[34]}$ 





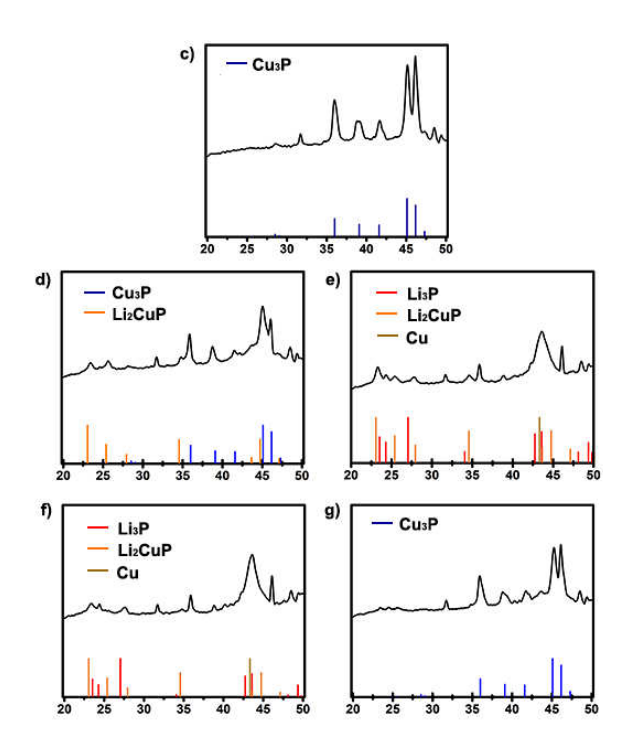


Figure 3. (a) Waterfall diagram showing the evolution of the in situ XRD patterns of the  $Cu_3P$  electrode upon the first lithiation/delithiation (scans 1-90) from 2.045 V to 0.01 V and back to 2.0 V. (b) The cyclic voltammogram plot of the pristine  $Cu_3P$  electrode at a scan rate of 0.025 mV s<sup>-1</sup>. (c) The 1<sup>st</sup> scan XRD pattern at 2.0 V,  $Cu_3P$  (PDF No. 04-010-6017) peaks are identified. (d) The 22<sup>nd</sup> scan XRD pattern 1.0 V,  $Li_2CuP$  (PDF-04-014-6306) peaks are identified. (e) The 38<sup>th</sup> scan XRD pattern at 0.36 V,  $Li_3P$  (04-014-7866),  $Li_2CuP$  (PDF-04-014-6306) and Cu (04-010-6011) peaks are identified (f) The 46<sup>th</sup> scan XRD pattern at 0.01 V with,  $Li_3P$  (04-014-7866),  $Li_2CuP$  (PDF-04-014-6306) and Cu (04-010-6011) peaks identifiedy. (g) The 90<sup>th</sup> scan XRD pattern at the voltage of 2.0 V.

In situ XRD analysis was also carried out to identify the first lithiation/delithiation process of Sn<sub>4</sub>P<sub>3</sub> material, the results are showed in Figure 4a. The XRD patterns acquired between 2.0 V and 0.01 V were recorded, and the 1<sup>st</sup>,  $30^{th}$ ,  $35^{th}$ ,  $40^{th}$ ,  $46^{th}$  and  $90^{th}$  scan at 2.0, 0.71, 0.48. 0.26, 0.01 and 2.0 V are shown in Figure 4c, 4d, 4e, 4f, 4g and 4h, respectively. The cyclic voltammogram of the pristine Sn<sub>4</sub>P<sub>3</sub> electrode is shown in Figure 4b. During the cathodic scan, the delithiation process of Li<sub>3</sub>P starts at about 1.0 V. It can be seen from Figure 4a that no phase change occurs from the initial state to 1.0 V. When the voltage decreases to 0.71 V, LiP  $(PDF\ 04-004-8721)$ ,  $^{[37]}\ Li_3P\ (PDF\ 04-014-7866)$  and  $Sn\ (PDF\ 04-009-6172)$  phases can be identified, [38] as shown in Figure 4d. The layered structure of Sn<sub>4</sub>P<sub>3</sub> phase disappears, which corresponds to the appearance of Sn<sup>0</sup> and the formation Li-P compounds (Li<sub>3</sub>P and LiP). Further delithation leads to alloying between Li and Sn, which agrees with Figure 4e at the voltage of 0.48 V in which no Sn phase can be seen. [14] These reactions correspond to the first wide peak (with unobvious shoulders) at 0.62 V in CV curve. As the lithiation process continues, several Li-Sn alloy such as  $\text{Li}_2\text{Sn}_5$  (PDF 04-005-5077), Li<sub>5</sub>Sn<sub>2</sub> (PDF 04-007-1468), Li<sub>7</sub>Sn<sub>2</sub> (PDF 04-004-8599), Li<sub>17</sub>Sn<sub>4</sub> (04-009-8644), Li<sub>22</sub>Sn<sub>5</sub> (PDF-04-003-6446)<sup>[43]</sup> with poorly developed long-range order are formed, [44] as seen in Figure 4f and 4g, corresponding to the second peak at 0.21 V in CV curve. Figure 4a and 4f-4h indicate that after first cycle, the active material loses its long range order and the initial crystalline Sn<sub>4</sub>P<sub>3</sub> phase apparently cannot be recovered at the end of the delithiation. This can be explained due to the fact that the Li and Sn atoms cannot move effectively in these phases at room temperature to form long-range ordered structures. [45] or the formation of Li<sub>4.4</sub>Sn and

then back to Sn will result in a decrease/pulverization of the Sn particle which can result in amorphous compounds showing either no peaks or a very broad region in XRD pattern.

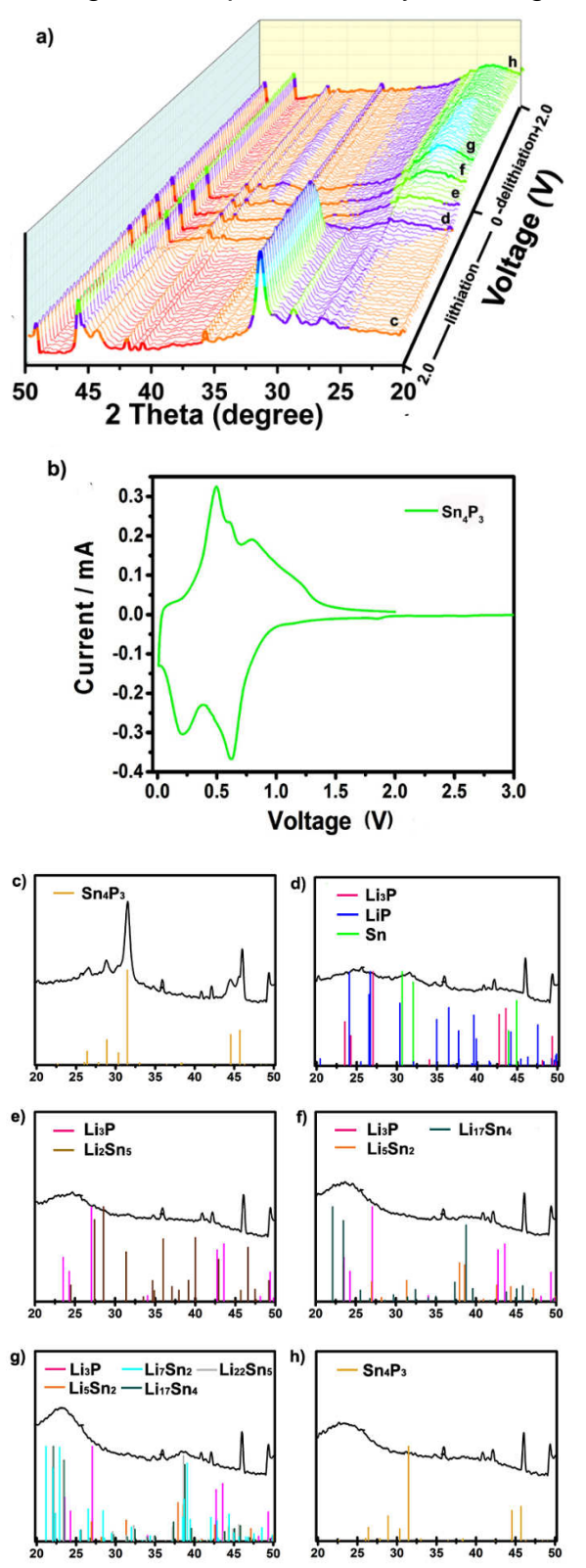


Figure 4. (a) Waterfall diagram of the in situ XRD patterns of the  $Sn_4P_3$  electrode upon the first lithiation/delithiation process in the voltage range of 2.0~V to 0.01~V. (b) The first cyclic voltammogram plot of the  $Sn_4P_3$  vs. Li at a scan rate of  $0.025~mV~s^1$ . (c) The  $1^{st}$  scan XRD pattern at 2.0~V,  $Sn_4P_3$  (PDF No. 04-003-2006) peaks are identified. [22, 29] (d) The  $30^{th}$  scan XRD pattern at 0.71~V, LiP (PDF 04-004-8721), [37] Sn (PDF 04-009-6172), [38]  $Li_3P$  (PDF 04-004-

014-7866) peaks are identified. (e) The  $35^{th}$  scan XRD pattern at 0.48~V,  $Li_3P$  (PDF 04-014-7866) and  $Li_2Sn_5$  (PDF 04-005- $5077)^{[39]}$  peaks are identified. (f) The  $40^{th}$  scan XRD pattern at 0.26~V,  $Li_3P$  (PDF 04-014-7866),  $Li_5Sn_2$  (PDF 04-007- $1468)^{[40]}$  and  $Li_{17}Sn_4$  (04-009- $8644)^{[42]}$  peaks are identified. (g) The  $46^{th}$  scan XRD pattern at 0.01~V,  $Li_3P$  (PDF 04-014-7866),  $Li_5Sn_2$  (PDF 04-007-1468), [40]  $Li_7Sn_2$  (PDF 04-004-8599),  $Li_{17}Sn_4$  (PDF04-009-8644) and  $Li_{22}Sn_5$  (PDF-04-003- $6446)^{[43]}$  peaks are identified. [41, 42] (h) The  $90^{th}$  scan XRD pattern at 2.0~V.

To observe the morphological changes of the Cu<sub>3</sub>P and Sn<sub>4</sub>P<sub>3</sub> electrodes during the lithiation/delithiation process, in situ SANS measurement was utilized for real-time characterization. Figure 5 shows the scattering result when the cells were discharged to 0.01 V. The data has been corrected for background and transmission, and were calibrated to absolute units by the secondary standard Plexiglas. All data have been radially averaged, since the scattering was isotropic. The major changes of the scattering for both samples relate to the contact region between the particle of active material and electrolyte. A dominant scattering feature at the low-Q-range is the ~Q-4 power law behavior, which is characteristic of a Porod scattering law due mostly to interfacial contributions (at length scales far above 10 nm) from the active material surface and the interface between particle and electrolyte [46], but also of time-independent contributions from other inactive materials such as conductive carbon, organic binder and separator. The calculated scattering length densities (SLDs) of various cell components are shown in Table S1. The obtained neutron scattering signal is a superposition of the individual scattering involving all cell parts: active material particles, conductive carbon, organic binder, separator, electrolyte and lithium foil. The time dependent fraction is attributed to the surface for overall particle of the electrode towards the electrolyte. Apart from that, an additional scattering contribution attributed to globular structures of ca. 8nm diameter growing at this interface with typical sizes well above 10 nm, a kind of surface decoration by the Beaucage model [beau] with a fixed exponent 4 for well-defined surfaces. [47] This decoration results from the volume expansion of the electrode material in terms of cracks and protrusions, that effectively appear as globules. The final scattering model reads as equation [1]:

$$\frac{d\Sigma}{d\Omega}(Q) = A_{\text{Porod}}Q^{-4} + A_{\text{globule}}\left(\exp\left(-\frac{1}{3}Q^{2}R_{g}^{2}\right) + \frac{8 \cdot \text{erf}^{12}(1.06QR_{g}/\sqrt{6})}{Q^{4}R_{g}^{4}}\right)$$
[1]

The deviations at larger  $Q > 0.1 \mbox{\mbox{\mbox{$A$}}}^{-1}$  can come either from a wrong fractal structure of the globular particles (~3) or from other globular particles with a different size. At higher  $Q \sim 0.5 \mbox{\mbox{\mbox{$A$}}}^{-1}$ , for both samples, a scattering peak might indicate a periodic structures. Since the latter two effects are well below the incoherent background level, we focused the interpretation on the two amplitudes  $A_{Porod}$  and  $A_{dlobule}$ .

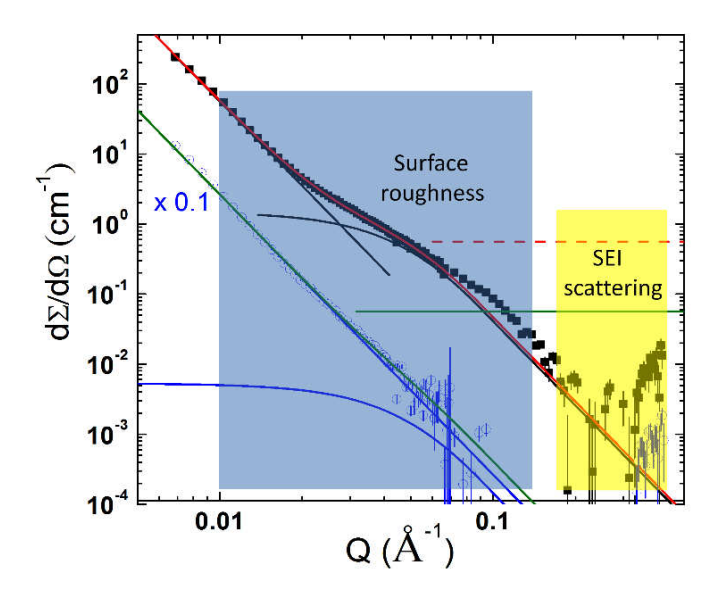


Figure 5. Scattering functions obtained from the in situ SANS measurement for  $Cu_3P$  (black) and  $Sn_3P_4$  (blue) electrodes lithiated to 0.01~V. Total fitting functions (red and green), the incoherent background (horizontal lines in red/ dashed and green/solid) and their separated two components (Porod and globular particles, both black and blue) are indicated.

In addition, the morphology changes of these electrodes at different states (pristine state.) lithiated to 0.01 V and delithiated back to 2 V) in the first discharge/charge process were evaluated by SEM with the corresponding EDX mapping for elemental distribution, as shown in Figure S1. In the pristine electrode, the Cu<sub>3</sub>P primary particles still remain agglomerated into secondary particle in the size of larger than 10 µm. EDX mapping images (Figure S1b and S1c) indicate that both Cu and P elements are homogeneously distributed. The fitting parameters of the SANS curves for the Cu<sub>3</sub>P sample (Figure 6a, b) showed a stable A<sub>Porod</sub> from 3.3 V to 1.2 V, indicating no obvious morphology change during lithiation above 1.2 V. In agreement wih in situ XRD results (Figure 3a), no structure changes and new phase can be seen before 1.2 V. When the cell is lithiated further to 0.01 V, the A<sub>Porod</sub> value decreases (Figure 6a, black rectangles), which indicates an overall surface area reduction of the active material particles. This suggests a uniform coating of the SEI on the surface of the active material particles which may also partly fills the void space between each small grain. For A<sub>alobule</sub> (black rectangles in Figure 6b), an increase is observed when the cell is discharged below 0.5 V (Figure 6b). This change is most likely due to the formation of small grains such as Cu<sup>0</sup> and Li<sub>3</sub>P, and the relative smaller structure of SEI molecules. The SEM image of the fully lithiated Cu<sub>3</sub>P electrode, shown in Figure S1d, illustrate the smoother surface formed. It may due to that a mixture of compounds of SEI and the products from active material at fully lithiated state (including Li<sub>x</sub>P and Cu<sup>0</sup>) are formed on the particles surface in the individual well separated small grains. Upon delithiation, the surface area increases (Figure 6a, red circles) as well as the amount of small grain (Figure 6b, red circles), which suggests the formation of the Li<sub>x</sub>Cu<sub>v</sub>P intermediate phases as a first step of Cu and Li<sub>3</sub>P delithiation. When Cu and Li<sub>3</sub>P are fully reacted, A<sub>alobule</sub> is restored to the pristine value. Li<sup>+</sup> ions are fully extracted from the Li<sub>x</sub>Cu<sub>y</sub>P intermediate phase, resulting in Cu<sub>3</sub>P at the end of delithiation process. EDX mapping images support this hypothesis as well, even though the Cu and P elements are mainly concentrated in the central region of the secondary particle at the end of lithiation due to the formation of the Li<sub>3</sub>P and Cu<sup>0</sup> (Figure S1e and S1f), the distribution is very homoigeneous as can be seen at the end of delithation (Figure S1h and S1i).

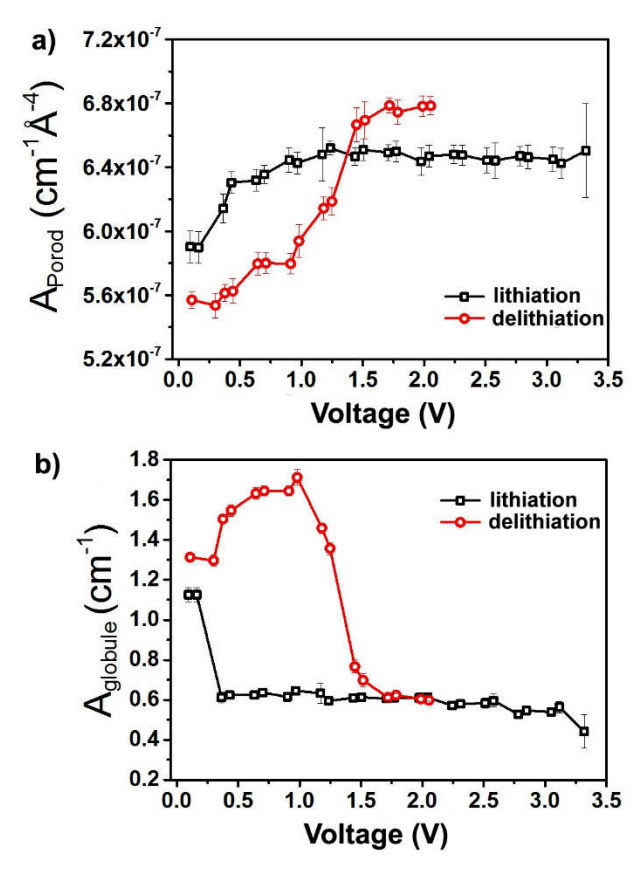


Figure 6. The fitting parameters of the SANS curves (a)  $A_{Porord}$  and (b)  $A_{globule}$  as a function in the voltage range of 0.01~V to 2~V at a sweep rate of  $0.2~mV~s^{-1}$ .

The electrochemical morphological changes of the Sn<sub>4</sub>P<sub>3</sub> electrode were also characterized by in situ SANS measurement. Figure 7 shows the fitting parameters Appropriate and Adoptile for a Sn<sub>4</sub>P<sub>3</sub> contained cell during the first cycle. Figure S2 shows SEM image and EDX mapping of the pristine Sn<sub>4</sub>P<sub>3</sub> electrode and the electrodes at different electrochemical lithiation states. As illustrated in Figure S2a particles with various sizes can be observed. EDX mapping performed on a small area of the composite electrode's surface, as shown in Figure S2b and S2c, indicates that both Sn and P elements are uniformly distributed. Up to the lithiation state of 1.0 V, the A<sub>Porod</sub> value corresponding to the surface morphology of Sn<sub>3</sub>P<sub>4</sub> electrode keeps steady (Figure 7a, black rectangles). However, as the lithiation continues, a slight increase of A<sub>Porod</sub> indicates a larger surface area or a rougher active material surface. Although the formation of SEI causes, in principle, a smoother surface, the SEI, in this case, cannot be maintain as a highly cohesive surface against large volume expansion experienced by the active material particles during cycling. As being discussed in the CV experiment, in contrast with the Cu<sub>3</sub>P electrode, Li<sup>+</sup> ions can further react with Sn to form a intermetallic phases (such as Li<sub>4.4</sub>Sn), resulting in more than 420% volume expansion. The mechanical failure of Sn<sub>4</sub>P<sub>3</sub> material during the lithiation process is expected to arise as a result of such large volume expansion. Thus, cracks occur and lead to a non-uniform chemical composition of the surface film, and become a preferred location for intensive Li deposition acting as nucleation points for Li dendrite formation. [48, 49] The overall slight increase of A<sub>Porod</sub> results from a compensation of crack formation and SEI filling. No small particles form on the surface after the lithiation process (Figure 7b, black rectangles), thus further demonstrates that the particles for both Li<sub>x</sub>Sn and Li<sub>3</sub>P were largely expanded. Figure S2d also shows relatively bigger particles in the lithated electrode compared to the pristine one. During delithiation, Li<sup>+</sup> ions are extracted from the swollen structures and this process creates additional detached domains that contribute to a considerable larger surface (Figure 7a, red circles) and also explain the formation of small grains (Figure 7b, red circles). The appearance of the small grains on the surface may be due to the delithiation of the disintegrated particles as observed in Figure S2g.

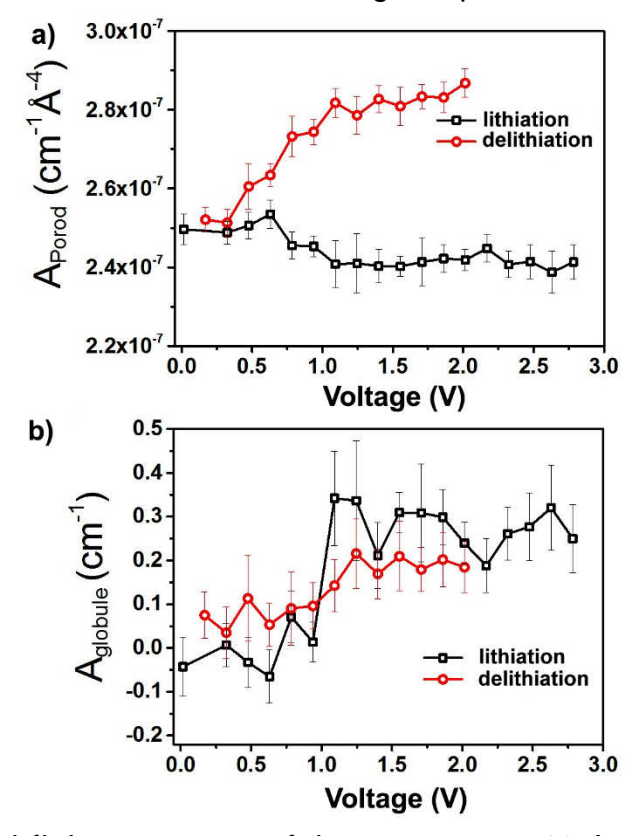


Figure 7. The essential fitting parameters of the SANS curves (a)  $A_{Porord}$  and (b)  $A_{globule}$  as a function in the voltage range of 0.01~V to 2~V at a scan rate of  $0.2~mV~s^{-1}$ .

Based on these observations, schematic drawings describing the reaction mechanisms and electrochemical morphology changes of  $Cu_3P$  and  $Sn_4P_3$  are depicted in the inset of Figure 8. Figure 8a revealed that the surface morphology changes of the  $Cu_3P$  during electrochemical process is mainly attributed to the formation of homogenous SEI layer and small grains and/or small cracks between the electrode and electrolyte due to the volume expansion during the lithiation. SEI leads to a smoother surface, but the volume shrinkage due to the lithium extraction from lithated electrode may lead to the interconnected cracks, which result in the increase in the  $A_{Porod}$  value (Figure 6b). Nevertheless, these changes do not harm the material structure, which is proved by in situ XRD that the  $Cu_3P$  phase can be restored at the end of the first cycle (i.e. at end of the first delithiation process).

Figure 8b illustrate the structural changes of  $Sn_4P_3$  during the first cycle. The large volume expansion destroys the SEI and results in cracks on the electrode surface as well. The lithiated electrode shows totally different morphology compare to the pristine electrode. As the electrochemical process goes on, the active material particles break up into several individual pieces and lose contact with the current collector. The nano-sized grain particles also lose their crystallinity and become amorphous, which was also detected by in situ XRD. On the micrometer scale the detachment of particles would lead to a fast fatigue of the electrode, because such particles of active material cannot contribute to the capacity of the cell anymore. Figure S4 displays local structure change for the cycled electrode, which provides an apparent evidence for the presence of chalking and dendrite growth. This observation is consistent with poor cycling performance of  $Sn_4P_3$ , as shown in Figure S5. Significant capacity fading in only S50 cycles originated from the serious structure collapse.

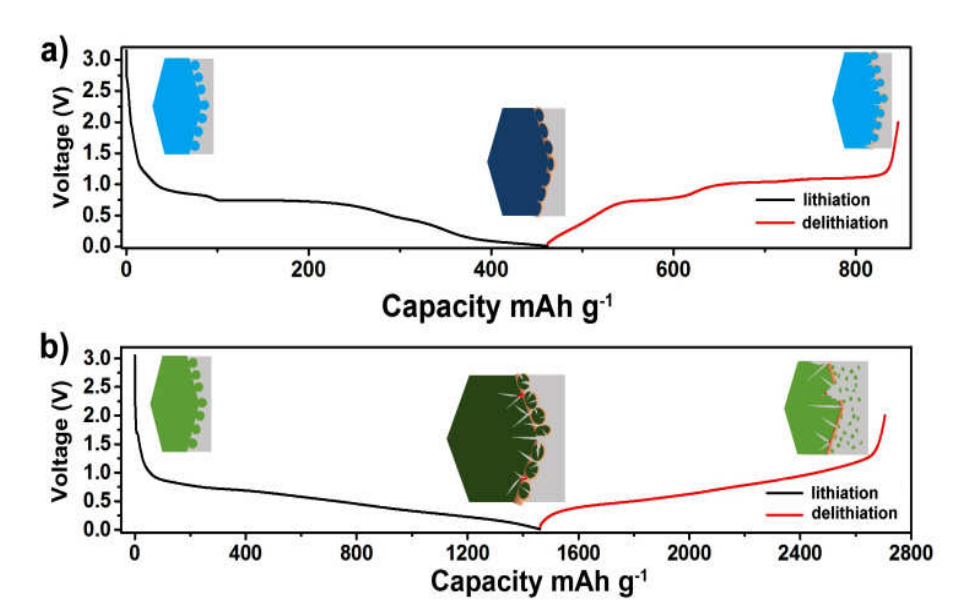


Figure 8. (a) Schematic of the morphology changes for the energy storage mechanism of  $\text{Cu}_3\text{P}$  sample at different stage in the  $1^{\text{st}}$  cycle in the voltage range of 0.01 - 2 V using a current density of 40 mA  $g^{-1}$ . (b) Schematic of the morphology changes for the energy storage mechanism of  $\text{Sn}_4\text{P}_3$  sample at different stage in the  $1^{\text{st}}$  cycle in the voltage range of 0.01 - 2 V at the current density of 150 mA  $g^{-1}$ .

#### Conclusion

In situ small-angle neutron scattering was used to investigate the morphological changes of two metal phosphide materials during the initial electrochemical lihitation cycle. By coupling SEM observation of the electrodes at different electrochemical states, it is able to evaluate the reaction mechanism of the active materials, including the SEI formation, swelling and recovering of nanoparticles, cracks appearance and stripping at nanoscale. With in situ XRD measurement which detects and characterizes phase transition mainly occurring at various electrochemical states, the energy storage mechanism was further explained. During the lithiation process of the Cu<sub>3</sub>P and Sn<sub>4</sub>P<sub>3</sub> electrodes, the insertion of Li-ions into the active component causes a large tensile stress. In the case of Cu<sub>3</sub>P material, no further reaction between Li-ions and Cu occurred at high lithiation state (low potential), which limited the whole volume expansion and reduced the related stress. As a result, only some branch cracks form on the electrode surface at the end of first cycle, but the structure and morphology of the active materials are well maintained. For the Sn<sub>4</sub>P<sub>3</sub> electrode, although the electrochemically active Sn can further react with Li and significantly contribute to the specific capacity, it leads to larger volume changes and stress. The interconnected cracks could isolate part of active material from the current collector, and the active material was finally detached during the delithiation process.

These results provide new insights into the electrochemical nanostructural changes of materials which are used as anode for lithium ion batteries via conversion and alloying reactions. It can help to understand the electrochemical behavior of the materials and to further improve their electrochemical performance.

#### Supporting Information

Supporting Information is available from the Wiley Online Library or from the author.

### Acknowledgements

The authors kindly acknowledge the financial support of Federal Ministry of Education and Research (BMBF), Federal Ministry of Economic and Technology and Federal Ministry for the Environment (BMWi), Nature Conservation and Nuclear Safety (BMU) of Germany within the project KaLiPat (03EK3008). The neutron experiments benefit from the KWS-1 instrument of the FRM II neutron source at the Heinz Maier-Leibnitz Zentrum (MLZ) in Garching (Germany)

Received: ((will be filled in by the editorial staff))
Revised: ((will be filled in by the editorial staff))
Published online: ((will be filled in by the editorial staff))

### References

- [1] J. Tian, Q. Liu, A. M. Asiri, X. Sun, J. Am. Chem. Soc. 2014, 136, 7587.
- [2] J. Tian, Q. Liu, N. Cheng, A. M. Asiri, X. Sun, Angew. Chem. Int. Ed. 2014, 53, 9577.
- [3] Z. Pu, Q. Liu, C. Tang, A. M. Asiri, X. Sun, Nanoscale 2014, 6, 11031.
- [4] P. Jiang, Q. Liu, X. Sun, Nanoscale 2014, 6, 13440.
- [5] H. Yang, Y. Zhang, F. Hu, Q. Wang, Nano Lett. 2015, 15, 7616.
- [6] X. Zhu, M. Liu, Y. Liu, R. Chen, Z. Nie, J. Li, S. Yao, J. Mater. Chem A 2016, 4, 8974.
- [7] M. Liu, J. Li, ACS Appl. Mater. Interfaces 2016, 8, 2158.
- [8] S. Boyanov, K. Annou, C. Villevieille, M. Pelosi, D. Zitoun, L. Monconduit, Ionics 2008, 14, 183.
- [9] Y. Lu, J.-p. Tu, Q.-q. Xiong, Y.-q. Qiao, X.-l. Wang, C.-d. Gu, S. X. Mao, RSC Adv. 2012, 2, 3430.
- [10] D. C. S. Souza, V. Pralong, A. J. Jacobson, L. F. Nazar, Science 2002, 296, 2012.
- [11] M. Sun, H. Liu, J. Qu, J. Li, Adv. Energy Mater. 2016, 6, 1600087.
- [12] M. G. Kim, J. Cho, Adv. Funct. Mater. 2009, 19, 1497.
- [13] C.-M. Park, J.-H. Kim, H. Kim, H.-J. Sohn, Chem. Soc. Rev. 2010, 39, 3115.
- [14] Y.-U. Kim, C. K. Lee, H.-J. Sohn, T. Kang, J. Electrochem. Soc. 2004, 151, A933.
- [15] J. Cabana, L. Monconduit, D. Larcher, M. R. Palacín, Adv. Mater. 2010, 22, E170.
- [16] Y. Kim, H. Hwang, C. S. Yoon, M. G. Kim, J. Cho, Adv. Mater. 2007, 19, 92.
- [17] L. Ji, Z. Lin, M. Alcoutlabi, X. Zhang, Energy Environ. Sci. 2011, 4, 2682.
- [18] M. C. Stan, R. Klöpsch, A. Bhaskar, J. Li, S. Passerini, M. Winter, Adv. Energy Mater. 2013, 3, 231.
- [19] H. Pfeiffer, F. Tancret, M.-P. Bichat, L. Monconduit, F. Favier, T. Brousse, Electrochem Commun. 2004, 6, 263.
- [20] G. Derrien, J. Hassoun, S. Panero, B. Scrosati, Adv. Mater. 2007, 19, 2336.
- [21] J. Hassoun, G. Derrien, S. Panero, B. Scrosati, Adv. Mater. 2008, 20, 3169.
- [22] Y.-U. Kim, S.-I. Lee, C. K. Lee, H.-J. Sohn, J. Power Sources 2005, 141, 163.
- [23] G. Nazri, Solid State Ion. 1989, 34, 97.
- [24] M.-P. Bichat, T. Politova, H. Pfeiffer, F. Tancret, L. Monconduit, J.-L. Pascal, T. Brousse, F. Favier, J. Power Sources 2004, *136*, 80.
- [25] F. Orsini, A. Du Pasquier, B. Beaudoin, J. M. Tarascon, M. Trentin, N. Langenhuizen, E. De Beer, P. Notten, J. Power Sources 1998, 76, 19.
- [26] N. Liu, Z. Lu, J. Zhao, M. T. McDowell, H.-W. Lee, W. Zhao, Y. Cui, Nat. Nanotech. 2014, 9, 187.
- [27] M. J. Hollamby, Phys. Chem. Chem. Phys. 2013, 15, 10566.
- [28] R. O. Demchyna, S. I. Chykhrij, Y. B. Kuz'ma, J. Alloys Compd. 2002, 345, 170.
- [29] O. Olle, Acta Chem. Scand. 1970, 24, 1153.

- [30] O. Olofsson, Acta Chem. Scand. 1972, 26, 2777.
- [31] J. V. Zaikina, K. A. Kovnir, A. N. Sobolev, I. A. Presniakov, V. G. Kytin, V. A. Kulbachinskii, A. V. Olenev, O. I. Lebedev, G. V. Tendeloo, E. V. Dikarev, A. V. Shevelkov, Chem. Mater. 2008, *20*, 2476.
- [32] M. P. Bichat, T. Politova, J. L. Pascal, F. Favier, L. Monconduit, J. Electrochem Soc. 2004, 151, A2074.
- [33] B. Mauvernay, M. L. Doublet, L. Monconduit, J. Phys. Chem. Solids 2006, 67, 1252.
- [34] F. Poli, A. Wong, J. S. Kshetrimayum, L. Monconduit, M. Letellier, Chem Mater. 2016, 28, 1787.
- [35] O. Crosnier, C. Mounsey, P. S. Herle, N. Taylor, L. F. Nazar, Chem. Mater. 2003, *15*, 4890.
- [36] Y. Dong, F. J. DiSalvo, Acta Crystallographica Section E 2007, 63, i97.
- [37] W. Hönle, G. von Schnering #, Z. Kristallogr. 1981, 155, 307.
- [38] R. Kubiak, J. Less Common Met. 1986, 116, 307.
- [39] D. A. Hansen, L. J. Chang, Acta Cryst. B 1969, 25, 2392.
- [40] U. Frank, W. Müller, H. Schäfer, Z. Naturforsch. B 1975, 30, 1.
- [41] U. Frank, W. Müller, H. Schäfer, Z. Naturforsch. B 1975, 30, 6.
- [42] G. R. Goward, N. J. Taylor, D. C. S. Souza, L. F. Nazar, J. Alloys Compd. 2001, *32*9, 82.
- [43] O. G. I. Gladyeshevskii E.I., Kripyakevich P.I., Kristallografiya, Sov. Phys. Crystallogr. 1964, 9, 269.
- [44] E. Rönnebro, J. Yin, A. Kitano, M. Wada, S. Tanase, T. Sakai, J. Electrochem Soc. 2004, 151, A1738.
- [45] I. A. Courtney, J. R. Dahn, J. Electrochem. Soc. 1997, 144, 2045.
- [46] R. L. Sacci, J. L. Bañuelos, G. M. Veith, K. C. Littrell, Y. Q. Cheng, C. U. Wildgruber, L. L. Jones, A. J. Ramirez-Cuesta, G. Rother, N. J. Dudney, J. Phys. Chem. C 2015, *11*9, 9816.
- [47] G. Beaucage, J. Appl. Cryst. 1996, 29, 134.
- [48] Y. S. Cohen, Y. Cohen, D. Aurbach, J. Phys. Chem. B 2000, 104, 12282.
- [49] R. Bhattacharyya, B. Key, H. Chen, A. S. Best, A. F. Hollenkamp, C. P. Grey, Nat. Mater. 2010, 9, 504.

### The table of content

The different electrochemical mechanisms of Cu3P and Sn4P3 anode materials for lithium ion batteries ware investigated by coupling the SEM, in situ XRD and in situ SANS techniques. Due to the further alloying between metal and Li at high lithiated state, the  $Sn_4P_3$  shows much more surface particle cracks with the destruction of the SEI layer and the worse cycling life.

